Experimental demonstration of noninvasive transskull adaptive focusing based on prior computed tomography scans

J.-F. Aubry,[a] M. Tanter, M. Pernot, J.-L. Thomas, and M. Fink
Laboratoire Ondes et Acoustique, ESPCI, Université Paris VII, U.M.R. C.N.R.S. 7587,
10 rue Vauquelin, 75005 Paris, France

Developing minimally invasive brain surgery by high-intensity focused ultrasound beams is of great interest in cancer therapy. However, the skull induces strong aberrations both in phase and amplitude, resulting in a severe degradation of the beam shape. Thus, an efficient brain tumor therapy would require an adaptive focusing, taking into account the effects of the skull. In this paper, we will show that the acoustic properties of the skull can be deduced from high resolution CT scans and used to achieve a noninvasive adaptive focusing. Simulations have been performed with a full 3-D finite differences code, taking into account all the heterogeneities inside the skull. The set of signals to be emitted in order to focus through the skull can thus be computed. The complete adaptive focusing procedure based on prior CT scans has been experimentally validated. This could have promising applications in brain tumor hyperthermia but also in transcranial ultrasonic imaging. © 2003 Acoustical Society of America. [DOI: 10.1121/1.1529663]

I. INTRODUCTION

Extracorporeal ablation of human tumors using High-Intensity Focused Ultrasound (HIFU) has been intensively investigated during the past decades.[1–4] Prostate cancer is certainly the most suitable application:[5,6] the target is reached via an endorectal probe close to the prostate tissue. It is much more difficult to cure tumors located deeply in the tissues: in this case, parts of the emitted wave front will encounter regions with different acoustic velocities, and different absorption coefficients, so that the heating beam pattern will be degraded. The worst medium to focus through is certainly the skull, as it was first shown by White *et al.*[7] during investigations into echographic brain imaging, and Fry *et al.*[8,9] during investigations into brain hyperthermia: a large discrepancy between high acoustic velocity of the skull (about 3000 m s^{-1}) and the low velocity of brain tissues (about 1540 m s^{-1}) combined with a severe attenuation of ultrasound in the bone strongly degrade the beam shape.

Several methods have been developed to precisely focus through the skull. The most invasive method consists in removing the piece of the skull in regard of the emitting array of transducers. Such a method has been experimentally used on living rats and cats in the early 1970s.[10] More recently, thermally induced lesions in rabbit brains were also studied by using a craniotomy.[11] One can also correct the aberrations induced by the skull either by using a Time Reversal Mirror[12] or by time shifting.[13,14] In the case of Time Reversal Mirrors, prior to the treatment and taking advantage of the biopsy, which ensures that the tumor is malignant, a hydrophone could be inserted in the neighborhood of the tumor and used as a beacon. Once the diagnostic would be confirmed and the hydrophone removed, the time-reversed signals with amplitude compensation could be emitted in order

to correct both phase and amplitude aberrations induced by the skull. Then, steering the signals[15] would enable one to precisely heat the whole tumor spot by spot. A refined extension of this method is the use of a spatiotemporal inverse filter:[16] taking advantage of the biopsy, one could put a set of transducers along the path followed by the physician. Then, after recording the whole set of impulse responses coming from the set of transducers, one could perform a very accurate focusing: it has been shown experimentally at low power[17] that it was possible to reach the same focusing quality through a human skull as the one obtained in water: phase distortion and attenuation induced by the skull can be corrected.

Recently, the possibility to deduce the acoustic properties of the skull from MRI and CT images raised new hopes for noninvasive brain therapy. Hynynen *et al.*[18,19] proposed to use MRI images for extracting the skull profile, without information on the internal heterogeneities. Then, using a three-layer model (water outside the skull, skull, and brain inside the skull), they numerically highlighted the necessity to perform the phase correction to focus through the skull. They proposed to perform this correction by deducing the phase aberrations induced by the skull thanks to simulations with the three-layer model.[20] In this work, they highlighted that the model would be enhanced by taking into account the heterogeneities of the skull. As CT images can give the internal structure of the skull, it is definitely more suited for modeling the ultrasonic properties of the skull.[20–22] In order to take into account all the information of the CT images, we propose here to use a three-dimensional (3-D) finite differences numerical simulation of the complete wave equation. By taking into account the internal heterogeneities in density, speed, and absorption, this finite differences simulation tries to model all the defocusing effects highlighted by White *et al.*[7]

It will first be explained how the acoustic velocity, the
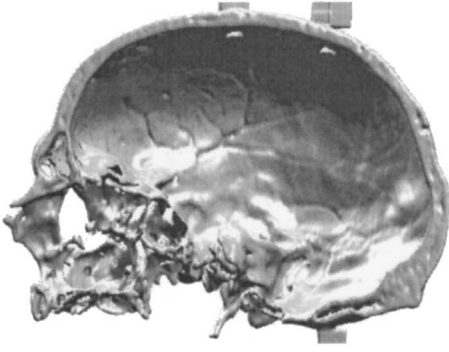
---

[a]Electronic mail: jf.aubry@espci.fr

FIG. 1. CT scan of the entire skull.

FIG. 2. Porosity map of a slice of the 3-D CT data.

density, and the absorption coefficient of the skull can be deduced from CT images. In Sec. II, comparisons between computed and experimental wave fronts passing through the same area of the same skull fully validate this model. Then, it will be shown in Sec. III that these results lead to noninvasive focusing through the skull. The focusing pattern obtained with a conventional time-reversal experiment is indeed close to the one experimentally obtained with our method based on simulations. Thus, by using CT images of the skull, it is possible to noninvasively correct both the phase and the amplitude aberrations induced by the skull. Beyond its interest for noninvasive brain therapy, full 3-D finite differences simulations are an interesting tool for modeling and understanding the complex acoustic wave propagation through bones.

II. ACOUSTIC PROPERTIES OF THE SKULL DEDUCED FROM CT IMAGES

It is known that cortical bones give no signal on Magnetic Resonance Imaging (MRI), whatever their density, but MRI is capable to provide the thickness of the skull. In this case, one can only model the acoustical properties of the skull with a uniform density, sound speed, and absorption. CT images can measure the internal density of the skull, enabling us to use more accurate models of the acoustical properties of the skull, taking into account the heterogeneities of density, sound speed, and absorption inside the skull.

A. CT images

High-resolution CT images have been performed at the Institut Français du Petrole (IFP), on a General Electric FXi model with a 0.2 mm in-plane spatial resolution. With transducers working at a central frequency of 1.5 MHz, it corresponds to a $\lambda/7$ precision in the skull, which is of great importance when trying to precisely simulate the wave propagation. The entire CT scan of the skull is given in Fig. 1. The scan parameters were set to 120 kV, 60 mA. Slices were 1 mm thick with a 0.5 mm pitch so that each slice was overlapping the previous one.

A dried human skull was midsagitally cut into two halves. In order to reproduce *in vivo* conditions as closely as possible, the skull is immersed in water and degassed so that no air bubble is trapped in porous zones. Instead of being filled with marrow, the porous parts of the skull are thus filled with water. However, it is important that those porous
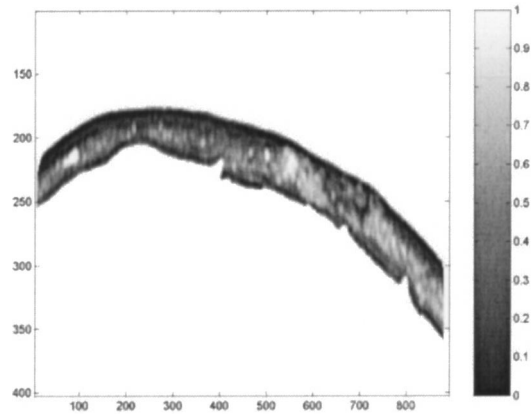
parts are not filled with air bubbles that would introduce artifacts in the CT scans. Raw CT values were given into Hounsfield Units (H), defined by

$$H = 1000 \frac{\mu_x - \mu_{\text{water}}}{\mu_{\text{bone}} - \mu_{\text{water}}}, \tag{1}$$

with μ_x, μ_{bone}, and μ_{water}, respectively, denoting the photoelectric linear attenuation coefficient of the explored tissue, bone, and water.

As the skull was placed in water and degassed, it is exclusively made of water and bone with a varying density. Consequently, Φ being the bone porosity, we propose here a linear relationship between the photoelectric linear attenuation coefficient of the explored tissue, and the attenuation coefficients of bone and water:

$$\mu_x = \Phi \mu_{\text{water}} + (1 - \Phi) \mu_{\text{bone}}. \tag{2}$$

In that case, the porosity map is directly linked to the Hounsfield map:

$$\Phi = 1 - \frac{H}{1000}. \tag{3}$$

Finally, all the acoustic properties (density, speed, and absorption coefficient) of the skull were deduced from the porosity maps. The porosity map of a slice is given in Fig. 2. Basically, the skull presents a three-layered structure, with a porous zone, called the diploe, stacked between two dense layers, respectively, the outer and inner tables. We can see that the diploe is very inhomogeneous and that it is sometimes hard to differentiate it from the tables.

B. Acoustic properties of the skull deduced from CT imaging

All the experiments were made with a plane linear array of 128 transducers working at a central frequency of 1.5 MHz, so that frequency ranges from 0.8 to 2 MHz. The elevation of the array (VERMON) is 1 cm, with a 0.5 mm pitch.
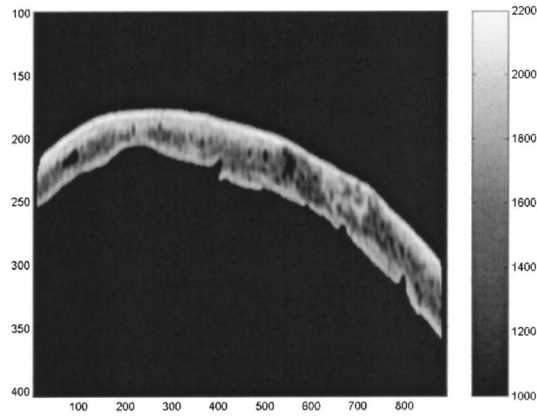
FIG. 3. Slice of the 3-D mass density map deduced from CT scans.

FIG. 4. Slice of the 3-D acoustic speed map deduced from CT scans.

1. Density

Mass density maps are easily deduced from the bone porosity:

$$d = \Phi \times d_{\text{water}} + (1 - \Phi) \times d_{\text{bone}}. \tag{4}$$

d_{water} is the mass density of water and has been set to 1000 kg m^{-3}; d_{bone} is the maximum mass density in the cortical bone. One can see that our simple model [Eq. (2) and Eq. (4)] implies a linear relationship between the bone density and the Hounsfield units, as observed experimentally by Rho et al.[23] and Ploeg et al.[24]

Fry et al.[25] statistically studied the acoustical properties of human skulls. They found an average mass density of 1900 kg m^{-3} in the inner table. Taking into account the heterogeneities inside the inner table, the maximum mass density of the cortical bone (d_{bone}) has thus been set to 2100 kg m^{-3} in order to obtain the same average mass density in the inner table as the one given by Fry et al. A slice of the 3-D mass density map is given in Fig. 3.

2. Speed of sound

The speed of sound is harder to deduce from the skull porosity. The diploe and the inner and outer tables have different mechanical properties.[25] Acoustic waves propagating in the fluid and the solid media are coupled, which is correctly described by the Biot theory if the wavelength is negligible compared to the size of the heterogeneities. At 1.5 MHz, the wavelength is unfortunately of the order of magnitude of the heterogeneities. However, Carter and Hayes[26] showed that the elastic modulus of bone is proportional to the apparent density cubed, which suggests a linear relationship between velocity and porosity:

$$c = c_{\text{min}} + (c_{\text{max}} - c_{\text{min}}) \times (1 - \Phi). \tag{5}$$

As porous parts are filled with water, c_{min} has been set to 1.5 mm μs^{-1}. Fry et al.[25] measured the same value in the inner and the outer table for the speed of sound: 2.9 mm μs^{-1}. According to this, c_{max} has been set to 2.9 mm μs^{-1}. A slice of the 3-D velocity map is given in Fig. 4. In order to give an idea of the entire 3-D velocity mesh used in the simulation, a representation is given in Fig. 5.
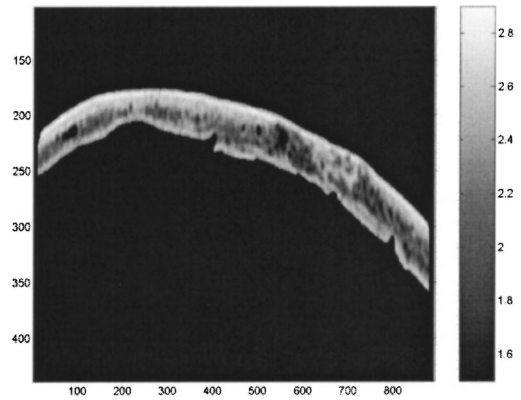
3. Absorption

As ultrasonic absorption is known to occur mainly in the diploe,[25] the absorption coefficient is expected to be a growing function of porosity. The following power law model was experimentally adjusted:

$$\text{abs} = \text{abs}_{\text{min}} + (\text{abs}_{\text{max}} - \text{abs}_{\text{min}}) \times (\Phi)^{\beta}. \tag{6}$$

Evaluating the mean absorption of wave fronts propagating through different parts of the skull showed that β could vary between 0.3 and 0.7. The best comparison between simulation and experiments were obtained with $\beta = 0.5$; abs$_{\text{min}}$ = 0.2 dB mm^{-1}; abs$_{\text{max}}$ = 8 dB mm^{-1}. This definitely sets the absorption coefficients for all the experiments performed through this skull. A slice of the 3-D absorption map is given in Fig. 6.

C. Numerical simulations

Simulations were performed with a finite differences program called ACEL developed in our lab. For 3-D simulations through the skull, a 20 h computational time is needed to compute a 70 mm $\times$ 10 mm $\times$ 30 mm box at an ultrasonic frequency of 1.5 MHz with a 500 MHz computer. Basically, the program is based on a discretization of the linear acoustic wave equation in heterogeneous absorbing media (7):

$$\left(1 + \tau_0(\mathbf{r}) \frac{\partial}{\partial t} \cdot\right) \left[\rho_0(\mathbf{r}) \nabla \cdot \left(\frac{1}{\rho_0(\mathbf{r})} \nabla p(\mathbf{r},t)\right)\right]$$
$$- \frac{1}{c_0(\mathbf{r})^2} \frac{\partial^2 p(\mathbf{r},t)}{\partial t^2} = S_0(\mathbf{r},t). \tag{7}$$

This equation accurately models fluids with sound speed, density, and absorption heterogeneities. Mode conversions and shear waves are not taken into account. Nevertheless, they can be neglected in a first approximation[25] as the wave front incidence angle on the skull's interface remains close to normal incidence. As the wavelength in the skull is larger than the inclusions, microstructures in the diploe are averaged by introducing an effective medium. In the bandwidth of the transducers, insertion loss increases as the second power of the frequency.[25] A second power frequency dependence of the insertion loss corresponds to a constant relaxation time,[28] as set in the simulation. In order to ensure a

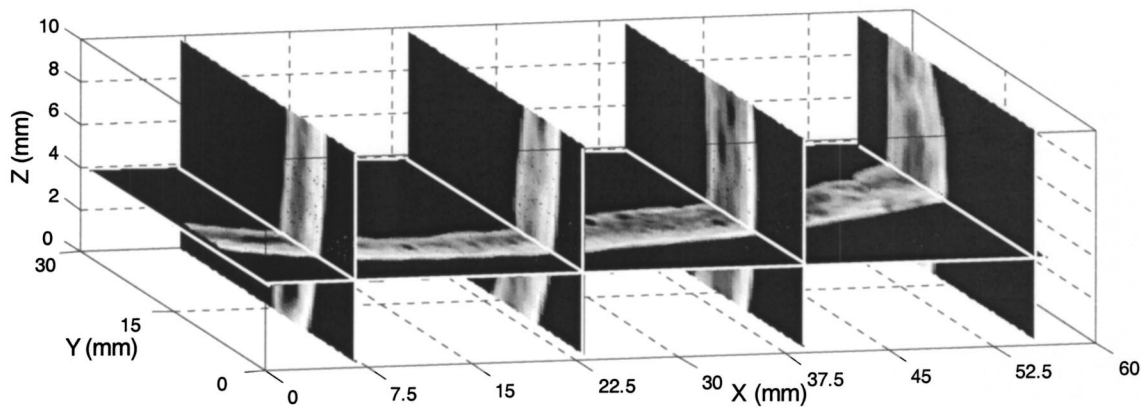Aubry et al.: Noninvasive transskull focusing

FIG. 5. A 3-D spatial representation of the sound speed distribution deduced from CT scans and used as input data in the full 3-D finite differences simulation (the box is 60 mm×30 mm×12.5 mm).

precise simulation, taking into account density, sound speed, and absorption heterogeneities, the spatial pitch is set to less than one-tenth of a wavelength and the time step is automatically set to ensure the von Neumann stability criteria.[29] Strongly absorbing boundary conditions based on a fourth-order approximation of Higdon conditions[30] are used at the sides and edges of the mesh to avoid unphysical reflections. Sets of receivers and emitters can be easily defined thanks to an intuitive graphic interface, as well as the velocity, density, and absorption maps [Eqs. (4), (5), and (6)] respectively, $c_0(\mathbf{r})$, $\rho_0(\mathbf{r})$, and $\tau_0(\mathbf{r})$. Then the numerical code propagates the wave front from the set of emitters to the set of receivers. The maps presented in Sec. II B were interpolated to one-tenth of a wavelength.

The position of the set of transducers on the simulation mesh is critical. It is indeed of great importance to carefully place the transducers at the same location in the simulations and in the experiment. Basically, the exact positions of three markers on the skull were recorded and the experimental configuration was reproduced with a one-millimeter precision in each direction. We did not notice significant degradation of the experimental focusing patterns based on simulations due to this variance in the estimation of the markers location. Further investigations could quantitatively estimate the effect of positioning errors.
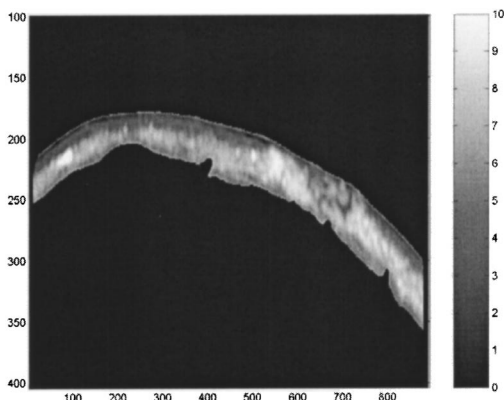
III. EXPERIMENTAL VALIDATION: COMPARISON BETWEEN COMPUTED AND EXPERIMENTAL WAVE FRONTS

The midsagitally cut human skull was placed between our linear array of 128 transducers and a needle hydrophone (Fig. 7). The whole experiment was immersed in water. In the general case, out of plane refractions have to be taken into account, explaining why a 3-D simulation code had to be computed. Nevertheless, we first tried to achieve a 2-D experiment by placing the needle hydrophone close to the skull. The surface of the skull has been aligned with the surface of our active elements in order to minimize refraction out of the simulation and experimental plane. Thus, first simulations could be performed in two dimensions, which is much more rapid. The hydrophone has a one millimeter external diameter housing and 0.5 mm diameter active surface ($\lambda/2$), so that one can assume that the experiment takes place in one slice of the CT scan (each slice is indeed 1 mm thick). A plane wave was emitted by the array of a transducer, and the hydrophone was translated along the x axis in order to record the wave front after passing through the skull. The plane wave front before passing the skull has also been recorded and is plotted in Fig. 8.

As expected, after propagation through the skull, the plane wave is strongly distorted, suffering both phase and amplitude distortions. The experimental wave front is presented in Fig. 9(a) and can be compared to the simulated one displayed in Fig. 9(b). At first glance, the simulation remarkably reproduces the influence of the skull. In Fig. 9(c) is reproduced the corresponding porosity map of the skull in
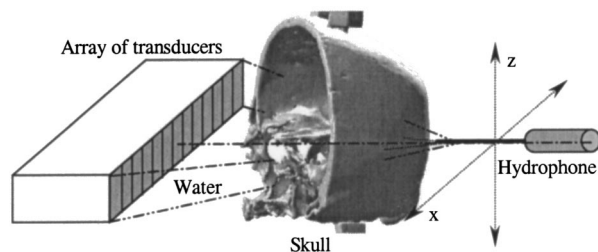

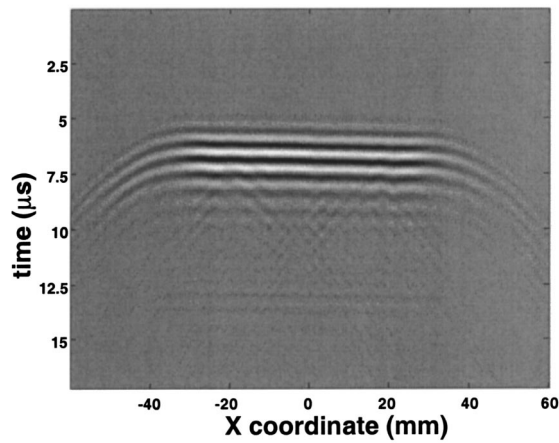FIG. 6. Slice of the 3-D absorption map deduced from CT scans.

FIG. 7. Experimental setup.

J. Acoust. Soc. Am., Vol. 113, No. 1, January 2003

Aubry *et al.*: Noninvasive transskull focusing   87

FIG. 8. Plane wave before passing through the skull (experiment).

a)

b)

FIG. 10. (a) Relative phase shift between the experimental and simulated plane wave propagating through the skull. (b) A comparison between experimental (dotted line) and simulated (solid line) normalized amplitude.

order to explain the influence of the skull. Two different zones have been highlighted. The zone one corresponds to a dense part of the skull with a relatively uniform absorption, so that the wave front is mainly distorted by the varying thickness of the skull, which is well reproduced on simulations. At position 40 mm on both experimental and simulated wave fronts, a dislocation can be seen: this is due to a notch [white arrow No. 2 in Fig. 9(c)] that acts like an acoustic lens.

A quantitative comparison between simulated and experimental wave fronts can be done. In Fig. 10(a) is plotted the relative time shifts between simulation and experiment. Time shifts have been evaluated by cross-correlating the signals of Figs. 9(a) and 8(b). In order to obtain a good focusing, Goodman[31] showed that the precision on the phase of the emitted signal should be less than T/8, where T is the period of the signal. One can see in Fig. 10(a) that this cri-
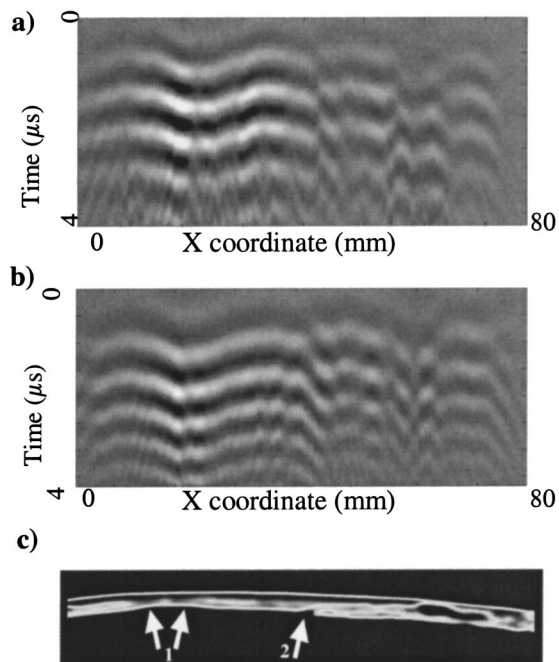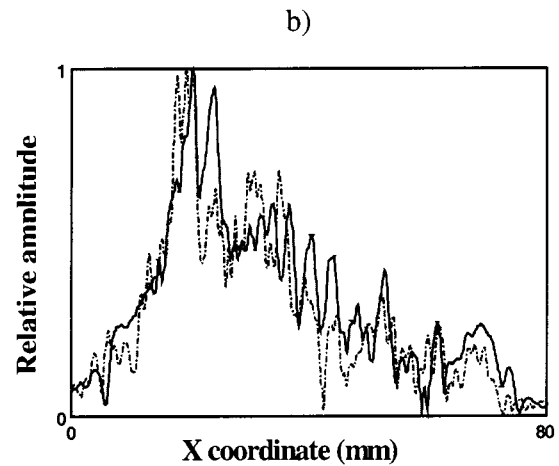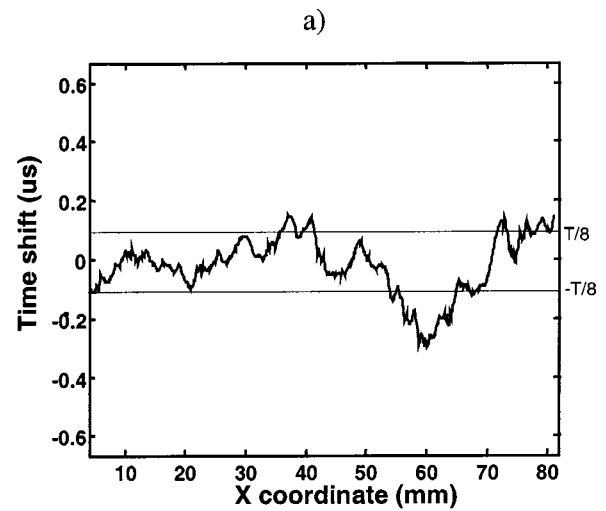
teria is well respected, except in one zone around position 60 corresponding to very low signal amplitude [see Fig. 9(a)]. Respective normalized amplitude at central frequency recorded or simulated at each location of the hydrophone are also plotted in Fig. 10(b) and are quite similar.

Studying the propagation of a plane wave through a human skull enabled us to validate the whole simulation process. In the following section, we will apply this process to perform noninvasive focusing through the skull.

IV. APPLICATION TO NONINVASIVE FOCUSING THROUGH THE SKULL

A. Experimental setup

The experimental setup, presented in Fig. 11, slightly differs from the one presented in Sec. II. Our aim is to determine the set of signals that have to be emitted on the array of transducers in order to obtain a sharp focusing. The quality of the focusing is experimentally checked by translating the hydrophone along the x axis and recording the maximum of pressure amplitude. In this section, as out of plane refrac-

a)

b)

c)

FIG. 9. Wave front after propagating through the skull: (a) Experiment; (b) simulation; (c) corresponding porosity map of the skull.
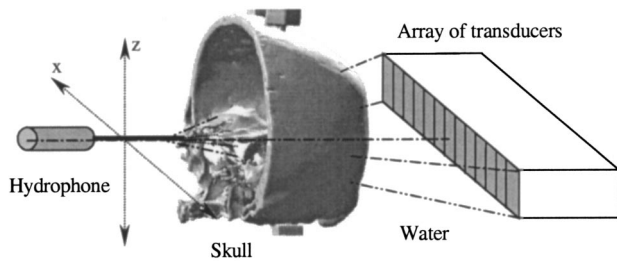
FIG. 11. Experimental setup.

tion effects have to be taken into account, all the simulations were performed with our full 3-D finite differences code. (See Fig. 12.)

B. Noninvasive time reversal

As seen in Sec. II, when focusing through the skull, parts of the wave front encounter regions with strongly different acoustic velocity and different absorption coefficient. This induces a severe spreading in the main lobe and an increase of the side lobes level, as one can see later in Fig. 14, showing the experimental directivity pattern obtained when focusing through the skull by emitting a cylindrical law with the array of transducers (dash–dotted line). This directivity pattern was obtained by plotting in a linear scale the square of the maximum of pressure amplitude recorded by the needle hydrophone at each location along the x axis. Such a focal spot is definitely not suited for brain hyperthermia: the maximum of pressure amplitude is not on the target (target at center) and the focusing quality is so poor that necrosis would also be induced in surrounding tissues.

Time reversal enables to correct the phase aberrations induced by the skull.[12] Basically, a pulse emitted by an acoustic source placed at the desired focus is recorded by an array of transducers after propagation through the medium. Then the recorded signals are time reversed and reemitted, so that the wave front propagates back to the source as if the

experiment was played backward. The experimental wave front coming from the central location of the hydrophone was recorded on the array of transducers and is presented in Fig. 13(a) after the time reversal operation. These time-reversed signals were experimentally reemitted by the array. We obtained the corresponding directivity pattern plotted in Fig. 14 (dotted line).

Thanks to simulations, it is possible to avoid the need of an ultrasonic source at focus by using a virtual source. An acoustic source was indeed placed on our CT images at the location of the desired focus. A pulse emitted by this virtual source was numerically propagated by the 3-D finite differences code through the skull to the array of transducers. This wave front numerically recorded on the array is presented after the time reversal operation in Fig. 13(b) and is very close to the one experimentally acquired [Fig. 13(a)]. The time-reversed simulated wave front was then experimentally emitted by the array of transducers. Finally, the experimental directivity pattern obtained by emitting the simulated set of signals is plotted in Fig. 14 (gray solid line). These experiments support the feasibility of totally noninvasive brain hyperthermia, since the focusing based on CT images (solid line) is close to the one obtained with a real acoustic source placed at the desired focus (dotted line): the focusing patterns are very similar, excluding an increase of the secondary lobe located at +10 mm from the center when using the simulated wave front. The strong defocusing effect observed when using a cylindrical law (dash–dotted line) is now well compensated for hyperthermia applications. Ebbini et al.[27] proposed an 8 dB side lobes amplitude as a threshold in order to avoid burning surrounding tissues. This is the case here.

In previous work, Thomas et al.[12] showed that at high frequencies (1.5 MHz) the focusing pattern could be strongly enhanced by combining time reversal with amplitude compensation. We will show in the following section that this can also be performed noninvasively.
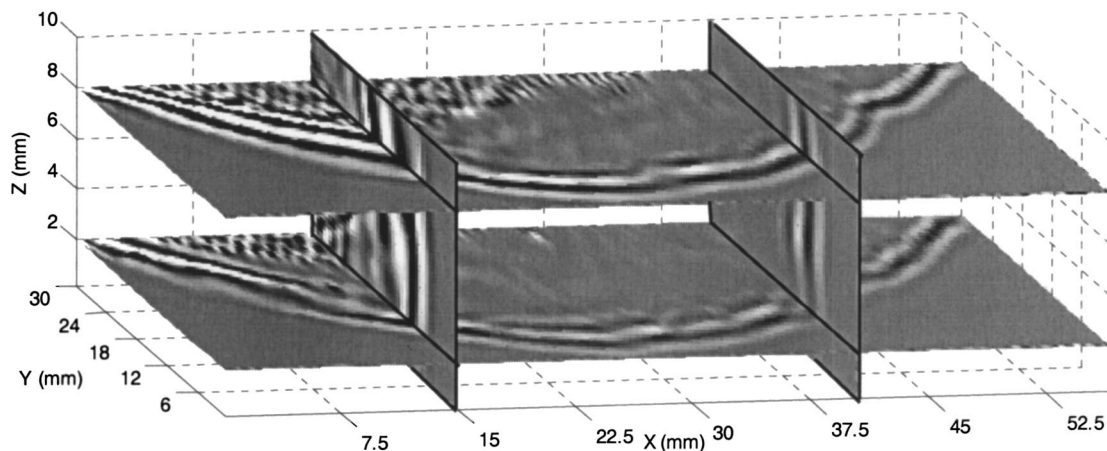

FIG. 12. Full 3-D finite differences simulation: 3-D spatial representation at a given time of the acoustic field passing through the skull (in a linear scale). The wave front is coming from a point-like source inside the brain. The calculation box (60 mm×30 mm×12.5 mm) corresponds to the 3-D volume presented in Fig. 5. One can notice some field variations along the elevation axis.
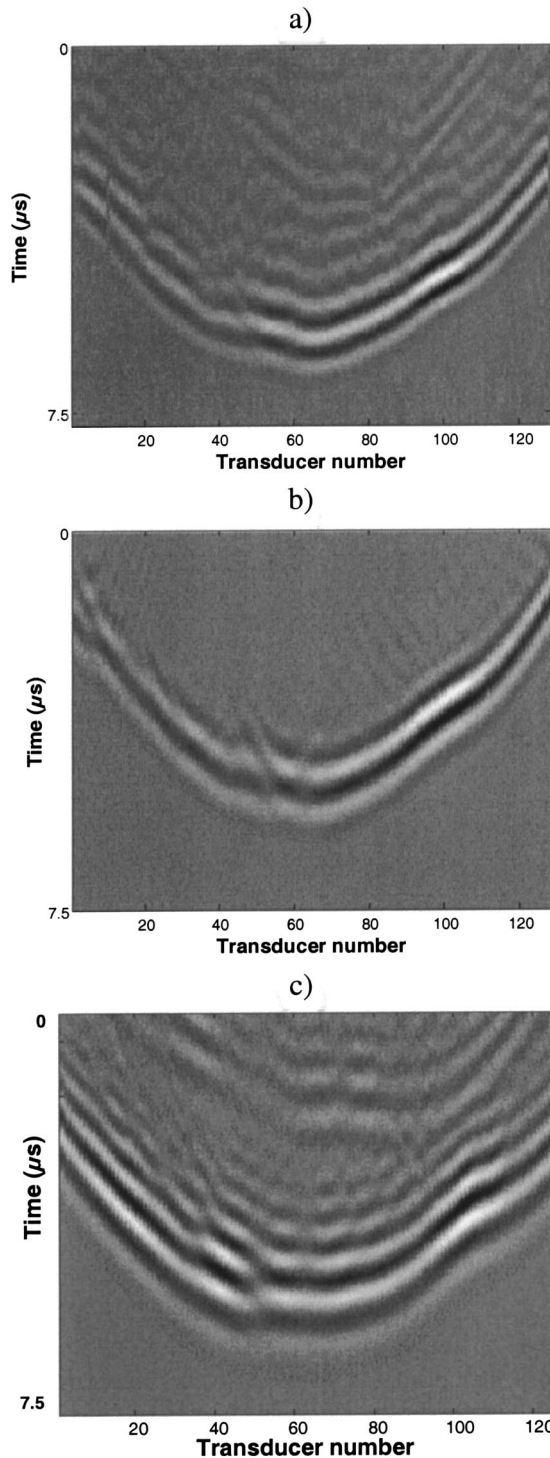
a)

b)

c)

FIG. 13. Time-reversed signals emitted by the array of transducers: (a) From experimental signals; (b) from the computed wave front (heterogeneous model); and (c) from a computed wave front (homogeneous model).
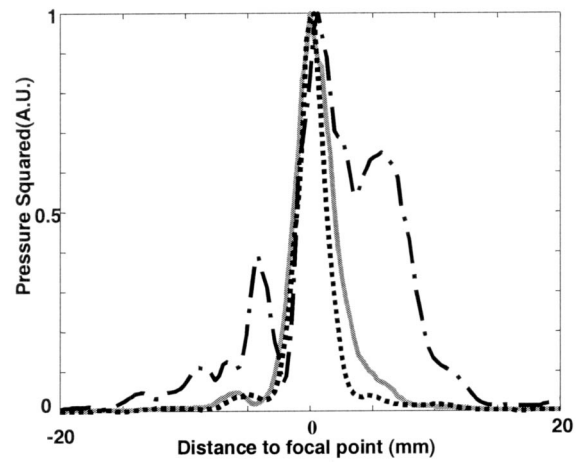

FIG. 14. Directivity pattern through the skull: energy (pressure squared) is plotted in a linear scale after emission of the time reversal of signals experimentally acquired (dotted line), of simulated signals (gray solid line), and of cylindrical law (dash–dotted line).

C. Noninvasive time reversal with amplitude compensation

Time reversal corrects phase aberrations induced by the propagating medium but does not correct amplitude aberrations. When focusing through a strongly absorbing medium like a human skull, the focusing can be improved by correcting the amplitude of the recorded signals.[12] This is particularly important when working at central frequencies above 1 MHz. The skull absorption is indeed increasing with the frequency, suggesting to work at low frequency. But decreasing the frequency also means decreasing the resolution and decreasing the heating of soft tissues, as their absorption coefficient is also increasing with the frequency. A compromise has to be determined. Hynynen *et al.* decided to work at low frequency to optimize the Specific Absorption Rate,[19] which is a good choice in order to avoid wasting energy in the skull. In that case, compensating the amplitude would only slightly improve the focusing, and a correct focusing can be achieved without amplitude correction. Another concern is the combination of HIFU and cavitation that may induce hemorrhages in the brain. As the cavitation threshold decreases with the frequency, hemorrhages are more likely to occur at low frequency. Our lab chose to work in a higher-frequency range (from 800 kHz to 1.5 MHz) for therapy, but also imaging. In that case, absorption effects become more important and an amplitude correction has been proposed.

Basically, assuming that the skull is an infinitely thin layer close to the emitting array of transducers, one can apply a gain on parts of the wave front that suffered a loss while passing through the skull. This so-called amplitude compensation is fully described in Ref. 12. The time-reversed signals obtained, respectively, by experiment and simulation presented in Fig. 13 were amplitude compensated (Fig. 15) and then were both experimentally emitted by the array of transducers. The corresponding focusing patterns are plotted in Fig. 16.

The focusing pattern obtained with a conventional time-reversal experiment with amplitude compensation is slightly better than the one based on simulations. More precisely, the right side has a lower level. Further work could show whether a better positioning system or a more precise adjustment of the parameters of the inhomogeneous model presented here could enhance the noninvasive process.

Either experimentally acquired or deduced from simulations, the focusing patterns obtained using time-reversal combined with amplitude compensation are much sharper since the effective aperture of the emitting array is enhanced.

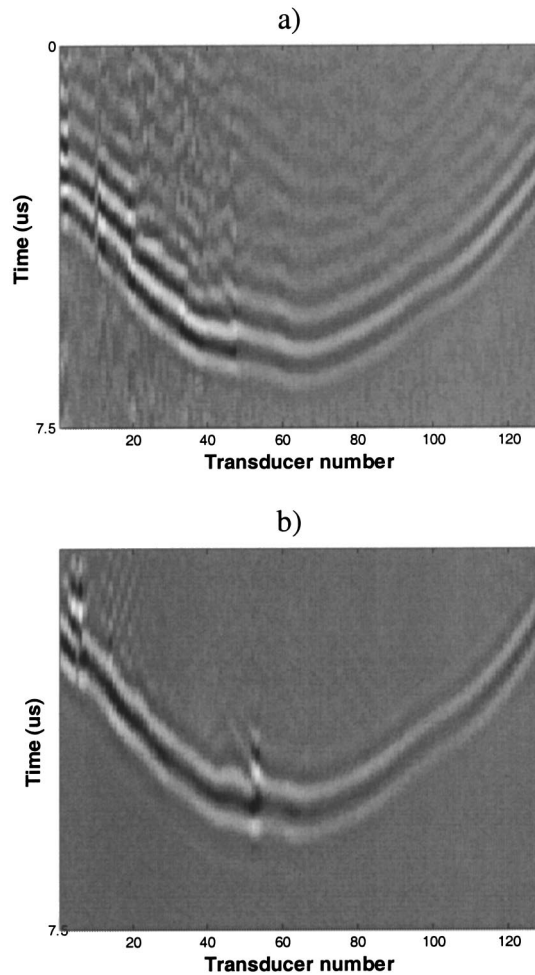Aubry *et al.*: Noninvasive transskull focusing

a)

b)

FIG. 15. Time-reversed signals with amplitude compensation emitted by the array of transducers: (a) From experimental acquisition and (b) from a computed wave front (heterogeneous model).
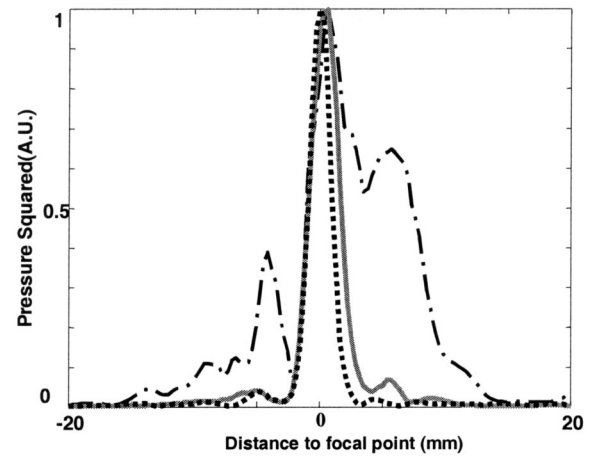

FIG. 16. The directivity pattern through the skull: energy (pressure squared) is plotted in a linear scale after the emission of time reversal with amplitude compensation of signals experimentally acquired (dotted line) and simulated signals (gray solid line) and of cylindrical law (dash–dotted line).

Moreover, the side lobe level is lower. Thus, the therapy will be more precise and tissues located in the near-field will be homogeneously insonified. Adding the amplitude compensation protects the brain tissues to the detriment of an overheating in the most absorbing parts of the skull. This overheating will be studied in further works.

D. Comparison with a homogeneous model

The full 3-D finite differences codes developed in this article take into account all the internal heterogeneities in density, speed, and absorption of the human skull detected on prior CT scans. A homogeneous model of the skull can also be proposed.[18,20] In a first approximation, one can indeed consider that the main effect of the skull results in its varying thickness, as the acoustic velocity and the density of the skull are about twice the velocity and the density of water and of the brain. In that case a fast simulation code can be used, based on ray tracing theory. In order to determine the advantage of taking into account the internal heterogenieties, other noninvasive focus have been conducted on other parts of the human skull. Two simulations of the wave front coming from a virtual source placed on the target were conducted: one with the previously presented heterogeneous model and one

with a homogeneous model. In the homogeneous model, according to the value deduced by Hynynen[20] from Fry et al.,[25] a mean velocity of 2.65 mm μs^{-1} has been taken, and a mean density of 1800 kg m^{-3}.

The emitted wave front was either not corrected or corrected thanks to the homogeneous or the heterogeneous model. They were emitted with the linear array of 128 transducers. The corresponding energy distributions are plotted in a linear scale in Fig. 17. One can clearly see that the homogenous model (dotted line) improves the focusing compared to a noncorrected wave front (dash–dotted line). The side lobes are significantly reduced, with a 10 dB gain. One can notice that the directivity pattern obtained with the homogeneous model is more symmetric and globally centered on the target, even if the maximum of pressure amplitude is not on the target: on this area of the skull, destructive interferences occur at the center. But the heterogeneous model developed in this article reaches a better focusing: the directivity pattern
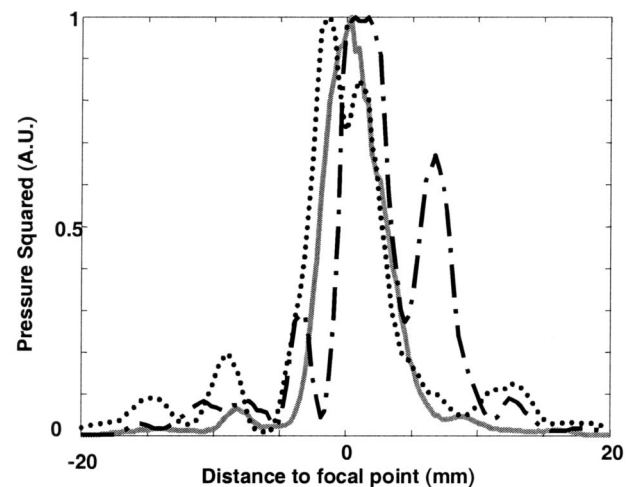

FIG. 17. Directivity pattern through the skull: energy (pressure squared) is plotted in a linear scale after the emission of cylindrical law (dash–dotted line), time reversal of simulated signals with heterogeneous model (gray solid line), and with a homogeneous model (dotted line).

is quite symmetric, the maximum of pressure amplitude is close to the target and the side lobes level are very low. Over 90 experiments conducted with various focusing techniques on various areas of the skull, the focusing capabilities were compared. Using a noncorrected wave front, a mean 1.5 mm absolute deviation from the target was observed, with a 0.2 mm standard deviation. With a noninvasive correction deduced from a homogeneous medium, the mean deviation decreased to 1.15 mm with a 0.2 mm standard deviation. The mean gain on the first side lobe was 6.2 dB, and 3 dB on the second side lobe. With a noninvasive correction deduced from a heterogeneous medium, the mean deviation decreased to 0.63 mm with a 0.3 mm standard deviation. Compared to noncorrected wave front, the mean gain on the first side lobe was 9.4, and 8.7 dB on the second side lobe. Thus, the heterogeneous model presented here shows a significant improvement, even if the homogeneous model shows good results compared to a noncorrected focusing. One also has to notice that the homogeneous model was solved here by using a finite differences code, taking into account higher refraction angles than codes derived from ray tracing theory. Moreover, the wave front coming from the virtual source has been simulated with the homogeneous model in the same configuration used in Secs. III B and III C. This wave front is presented in Fig. 13(c), and can be compared to the experimental one [Fig. 13(a)] and the one obtained with the heterogeneous model [Fig. 13(b)]. One can see that the amplitude of the wave front is not well reproduced. This means that such a model only allows performing time shifting or time reversal. With a more complex model like the heterogeneous one presented here, one can try to perform more complex focusing by changing the phase and the amplitude of the signals. Even if time shifting is necessary and has to be taken into account to perform brain hyperthermia,[19] new developments can be envisioned with a more accurate model, such as amplitude compensation.[12]

Of course, this first study has to be extended on other human skulls that the laboratory is currently looking for. The different models also have to be compared at lower frequencies, where the distortions induced by the skull are less important.

V. CONCLUSION

Based on prior CT scans, a 3-D finite differences numerical simulation of the complete wave equation has been proposed. This 3-D code takes into account the internal heterogeneities in density, speed, and absorption of the human skull. Thanks to this model, simulated wave fronts passing through the modeled skull are very close to the corresponding experimental wave fronts propagating through the same part of the skull. Moreover, the propagation through the skull of a wave front coming from a virtual point-like source located inside the brain can be simulated and recorded by a set of receivers. The same geometry is experimentally reproduced and the simulated wave front is time reversed and experimentally emitted by a real array of transducers. This enables us to achieve a complete time reversal experiment combined with amplitude compensation without the need of a physical source inside the brain, as the finite differences

code guided by CT scans allows us to create virtual sources inside the brain. As both phase and amplitude aberration induced by the skull can be noninvasively corrected, this technique could show encouraging promise in brain hyperthermia. A time reversal mirror made of 200 high-power transducers is under construction to bring into play this noninvasive hyperthermia protocol. Beyond its interest for noninvasive brain therapy, full 3-D finite differences simulations are an interesting tool for modeling and understanding the complex acoustic wave propagation through the skull.

[1] G. ter Haar, "Acoustic surgery," Phys. Today **54**, 29–32 (2001).

[2] K. Hynynen, O. Pomeroy, D. N. Smith, P. E. Huber, N. J. McDannold, J. Kettenbach, J. Baum, S. Singer, and F. A. Jolesz, "MRI imaging-guided focused ultrasound surgery of fibroadenomas in the breast: a feasibility study," Radiology **219**, 176–185 (2001).

[3] Feng Wu, W. Z. Chen, J. Bai, J. Z. Zou, Z. L. Wang, H. Zhu, and Z. B. Wang, "Pathological changes in human malignant carcinoma treated with high-intensity ultrasound," Ultrasound Med. Biol. **27**, 1099–1106 (2001).

[4] S. Vaezy, M. Andrew, P. Kaczkowski, and L. Crum, "Image-guided acoustic therapy," Annu. Rev. Bioeng. **3**, 375–390 (2001).

[5] T. Uchida, N. Sanghvi et al., "Transrectal high-intensity focused ultrasound for treatment of patients with localized prostate cancer: a preliminary report," Urology **59**(3) 394–399 (2002).

[6] A. Gelet, J. Y. Chapelon, R. Bouvier, R. Souchon, C. Pangaud, A. F. Abdelrahim, D. Cathignol, and J. M. Dubernard, "Treatment of prostate cancer with transrectal focused ultrasound: early clinical experience," Eur. Urol. **29**, 174–183 (1996).

[7] D. N. White, J. M. Clark, J. N. Chesebrough, M. N. White, and J. K. Campbell, "Effect of skull in degrading the display of echoencephalographic B and C scans," J. Acoust. Soc. Am. **44**, 1339–1345 (1968).

[8] F. J. Fry, "Transskull transmission of an intense focused ultrasonic beam," Ultrasound Med. Biol. **3**, 179–184 (1977).

[9] F. J. Fry and S. A. Goss, "Further studies of the transskull transmission of an intense focused ultrasonic beam: lesion production at 500 kHz," Ultrasound Med. Biol. **6**, 33–38 (1980).

[10] F. J. Fry, G. Kossof, R. C. Eggleton, and F. Dunn, "Threshold Ultrasonic dosages for structural changes in the mammalian brain," J. Acoust. Soc. Am. **48**, 1413–1417 (1970).

[11] N. I. Vykhodtseva, K. Hynynen, and C. Damianou, "Pulse duration and peak intensity during focused ultrasound surgery: theoretical and experimental effects in rabbit brain in vivo," Ultrasound Med. Biol. **20**, 987–1000 (1994).

[12] J.-L. Thomas and M. Fink, "Ultrasonic beam focusing through tissue inhomogeneities with a time reversal mirror: application to transskull therapy," IEEE Trans. Ultrason. Ferroelectr. Freq. Control **43**, 1122–1129 (1996).

[13] G. T. Clement, J. Sun, T. Giesecke, and K. Hynynen, "A hemisphere array for non invasive ultrasound surgery and therapy," Phys. Med. Biol. **45**, 3707–3719 (2000).

[14] G. T. Clement, J. P. White, and K. Hynynen, "Investigation of a large area phased array for focused ultrasound surgery through the skull," Phys. Med. Biol. **45**, 1071–1083 (2000).

[15] M. Tanter, J.-L. Thomas, and M. Fink, "Focusing and steering through absorbing and aberating layers: Application to ultrasonic propagation through the skull," J. Acoust. Soc. Am. **103**, 2403–2410 (1998).

[16] M. Tanter, J.-F. Aubry, J. Gerber, J.-L. Thomas, and M. Fink, "Optimal focusing by spatio-temporal inverse filter. I. Basic principles," J. Acoust. Soc. Am. **110**, 37–47 (2001).

[17] J.-F. Aubry, M. Tanter, J. Gerber, J.-L. Thomas, and M. Fink, "Optimal focusing by spatio-temporal inverse filter. II. Application to focusing through absorbing and reverberating media," J. Acoust. Soc. Am. **110**, 48–58 (2001).

[18] J. Sun and K. Hynynen, "Focusing of therapeutic ultrasound through a human skull: A numerical study," J. Acoust. Soc. Am. **104**, 1705–1715 (1998).

[19] J. Sun and K. Hynynen, "The potential of transskull ultrasound therapy and surgery using the maximum available surface area," J. Acoust. Soc. Am. **105**, 2519–2527 (1999).

[20] K. Hynynen and J. Sun, "Transskull ultrasound therapy: The feasibility of using image derived skull thickness information to correct the phase distortion," IEEE Trans. Ultrason. Ferroelectr. Freq. Control **46**, 752–755 (1999).

[21] G. T. Clement, C. Connor, and K. Hynynen, "Treatment planning for transskull focused ultrasound surgery and therapy," *Proceedings of the 17th International Congress on Acoustics*, 2001.

[22] M. Pernot, J.-F. Aubry, M. Tanter, J.-L. Thomas, and M. Fink, "Experimental validation of finite differences simulations of the ultrasonic wave propagation through skull," Proc. IEEE Ultrason. Symp. **2**, 1547–1550 (2001).

[23] J. Y. Rho, M. C. Hobato, and R. B. Ashman, "Relations of mechanical properties to density and CT numbers in human bone," Med. Eng. Phys. **17**, 347–355 (1995).

[24] H. Ploeg, W. Taylor, M. Warner, D. Hertig, and S. Clift, "FEA and bone remodelling after total hip replacement," awarded Best Paper Award, *Proceedings of the NAFEMS World Congress*, 2001, pp. 13–17. A version of this article is available online at ⟨http://www.nafems.org/publications/downloads/Bone%20Remodeling.pdf⟩.

[25] F. J. Fry and J. E. Barger, "Acoustical properties of the human skull," J. Acoust. Soc. Am. **65**, 1576–1590 (1978).

[26] D. R. Carter and W. C. Hayes, "The compressive behavior of bone as a two-phase porous structure," J. Bone Jt. Surg. **59A**, 954–962 (1977).

[27] E. S. Ebbini and C. A. Cain, "A spherical-section ultrasound phased-array applicator for deep localized hyperthermia," IEEE Trans. Biomed. Eng. **38**, 634–643 (1991).

[28] L. E. Kinsler, A. R. Frey, A. B. Coppens, and J. V. Sanders, *Fundamentals of Acoustics* (Wiley, New York, 1982), ISBN 0-471-02933-5, pp. 142–145.

[29] W. H. Press, S. A. Teukolsky, W. T. Vetterling, and B. P. Flannery, *Numerical Recipes in C* (Cambridge University Press, Cambridge, 1992), ISBN 0-521-43108-5, pp. 836–849.

[30] R. L. Higdon, "Absorbing boundary conditions for elastic waves," Geophys. Soc. Expl. Geophys. **56**, 231–241 (1991).

[31] J. W. Goodman, *Statistical Optics* (Wiley, New York, 1985).